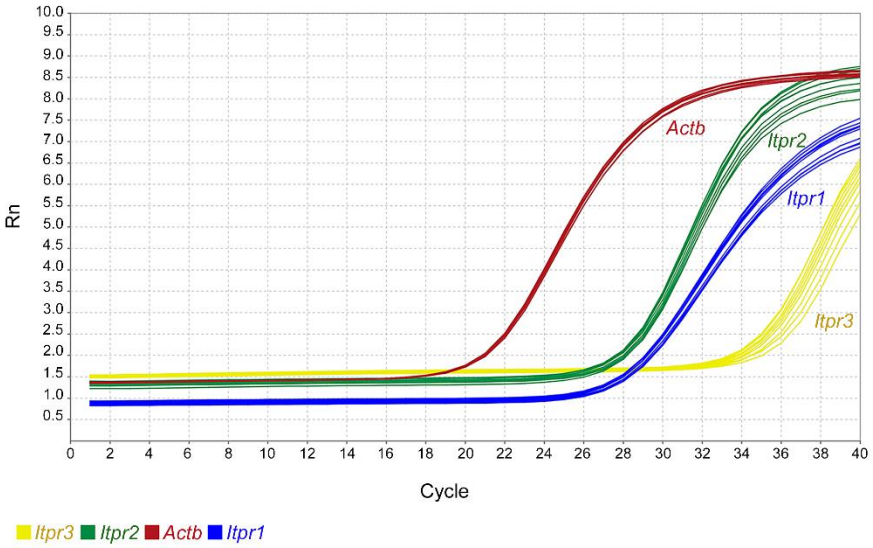
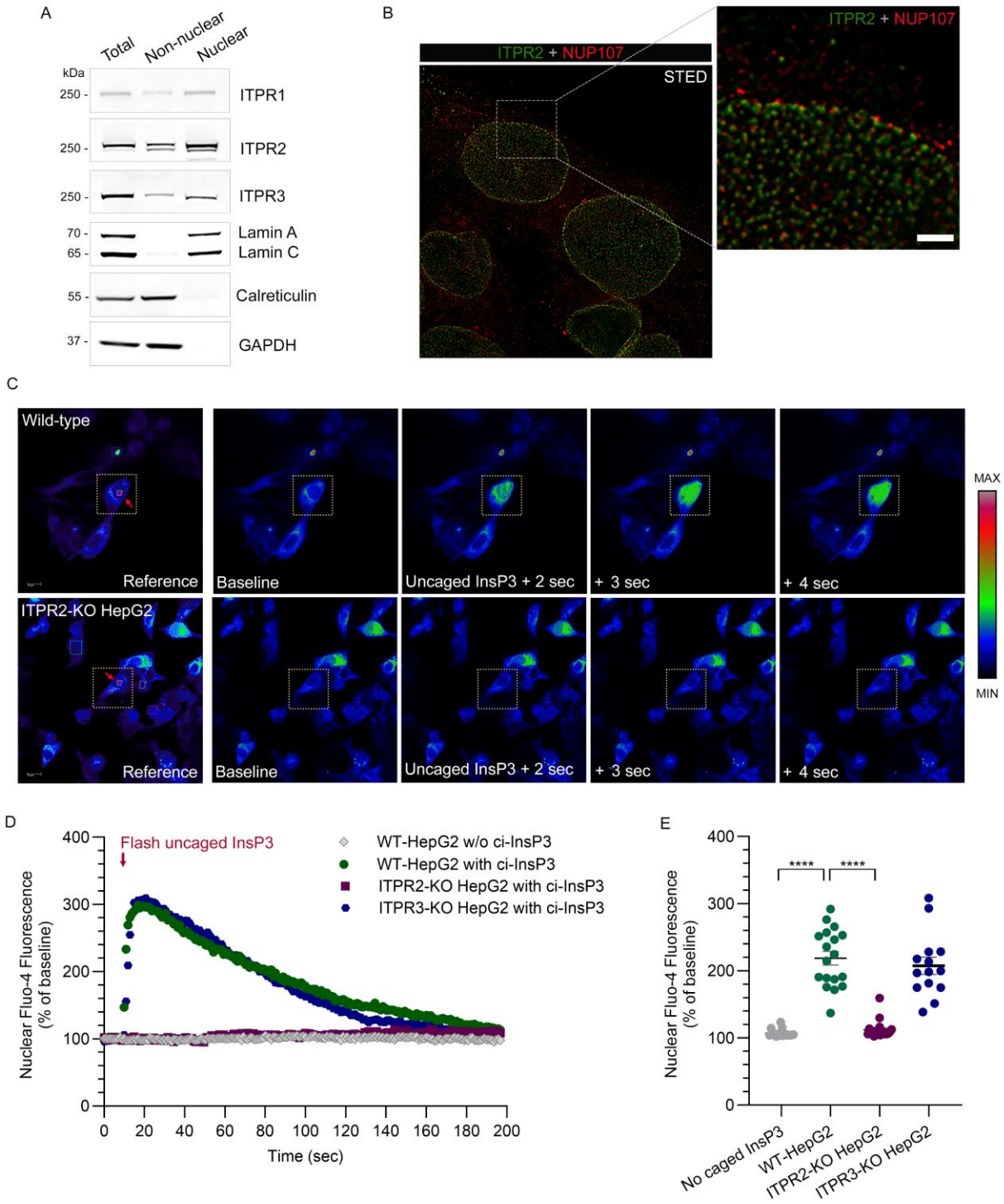
Impaired regulation of nuclear calcium signals is a driver of chronic liver disease

Jittima Weerachayaphorn, Mateus T. Guerra, Naotaka Kugiyama, Emma Kruglov, Dejian Zhao, Piyachat Chansela, Vitoon Saengsirisuwan, Marie E. Robert, Teruo Utsumi, Yasuko Iwakiri, Michael H. Nathanson

SUPPLEMENTAL FIGURES

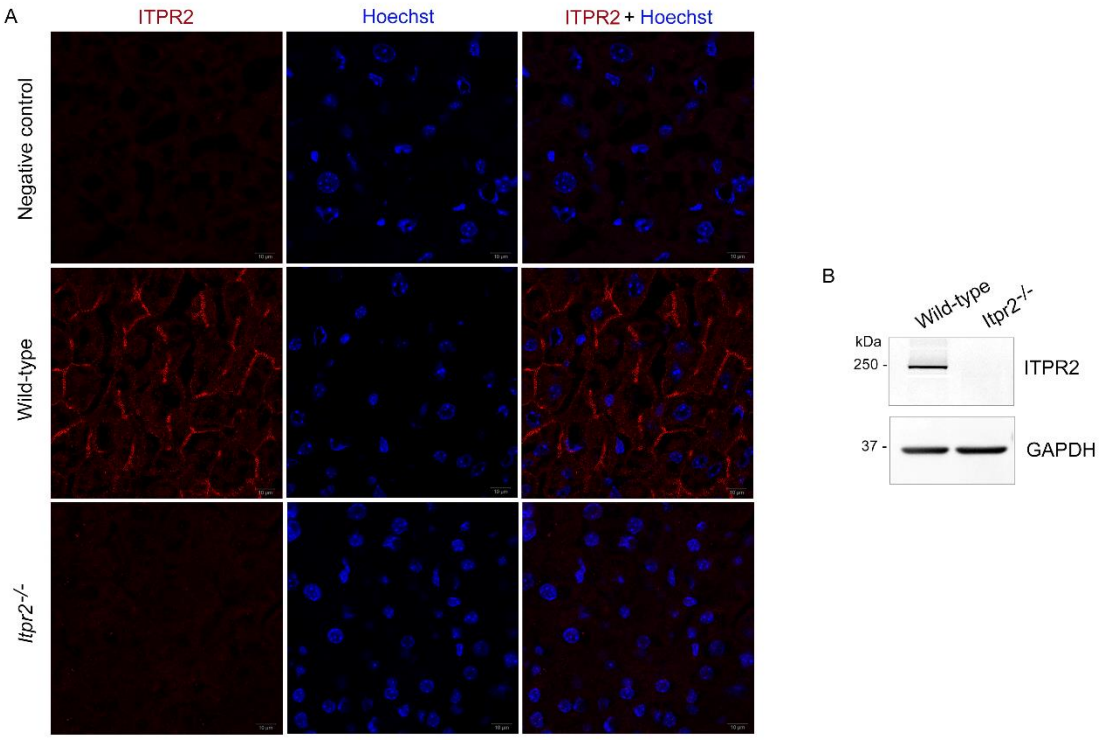


Supplemental Figure 1. Real-time quantitative PCR amplification plots confirm differential abundance of ITPR isoforms in mouse hepatocytes. ITPR isoform mRNA expression was analyzed by TaqMan real-time quantitative PCR (qPCR). Representative RT-qPCR amplification curves showing the relative abundance for ITPR isoforms obtained from primary mouse hepatocytes. The x-axis indicates the number of cycles, and the y-axis represents the fluorescence intensity above background. ITPR isoform 1 (*Itpr1*) amplification crossed the threshold at approximately 28.5 cycles, ITPR isoform 2 (*Itpr2*) at 27.8 cycles, and ITPR isoform 3 (*Itpr3*) at 35.1 cycles. *Atcb* amplification reached the threshold at approximately 21.2 cycles for all reactions. Earlier amplification indicates higher transcript abundance and *Itpr2* is the predominant isoform in primary mouse hepatocytes, as reported previously based on immunoblots.

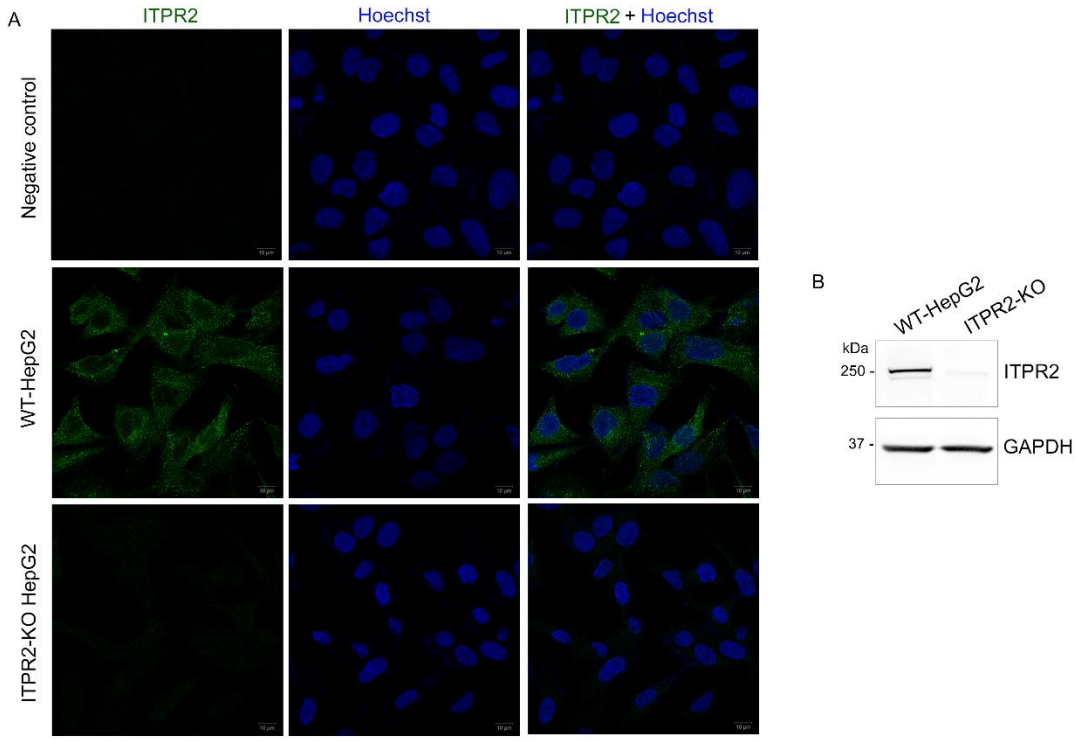


Supplemental Figure 2. ITPR2 is the principal isoform expressed in the nucleus of HepG2 cells and nuclear Ca^{2+} release is mediated through ITPR2. (**A**) Representative immunoblot of total whole cell, non-nuclear, and nuclear fractions for ITPR1, ITPR2 and ITPR3 expression. Total whole cell, non-nuclear, and nuclear fractions were isolated from HepG2 cells and analyzed by

immunoblotting with antibodies specific for ITPR1, ITPR2 and ITPR3. Lamin A/C was used as a nuclear marker, and calreticulin and GAPDH were used as non-nuclear (endoplasmic reticulum and cytosolic) markers to verify fractionation purity. (**B**) Minimal co-localization of ITPR2 and nuclear pore marker (NUP107) in HepG2 cells visualized by gSTED microscopy. Representative gSTED images show the subcellular distribution of ITPR2 (*green*) and NUP107 (*red*) in HepG2 cells. Note rare yellow labeling (co-localization) in the merged image. Magnified gSTED image showing distinct ITPR2 and NUP107 labeling, highlighted by the dotted square; scale bar 1 μm. (**C**) Serial confocal images of nuclear Ca^{2+} signals in representative wild-type and ITPR2-KO HepG2 cells. Cells were loaded with caged InsP3 (ci-InsP3) and Fluo-4/AM. ci-InsP3 was photo-released within the indicated region (small white square in the middle of the nucleus), as shown in a reference image of the designated cell (dotted large square), by a controlled near-UV (405 nm) flash and the induced nuclear Ca^{2+} signal was monitored by time-lapse swept-field confocal microscopy. A pseudo-colored Ca^{2+} scale is shown at right. (**D**) Representative tracings from single cells show an InsP3-induced increase in nuclear Ca^{2+} signals in wild-type, ITPR2-KO, and ITPR3-KO HepG2 cells. A much smaller increase in nuclear Ca^{2+} signals is seen in ITPR2-KO HepG2 cells, which is similar in magnitude to the small, nonspecific increase seen in a wild-type HepG2 cells subjected to the same near-UV flash but not loaded with ci-InsP3. (**E**) Quantitation of fluorescence shows that InsP3-induced nuclear Ca^{2+} signals are significantly decreased in ITPR2-KO but not ITPR3-KO HepG2 cells. Values reflect individual data points and mean ± SEM from wild-type without ci-InsP3 (17 cells), wild-type with ci-InsP3 (18 cells), ITPR2-KO HepG2 with ci-InsP3 (19 cells), and ITPR3-KO HepG2 with ci-InsP3 (14 cells). Statistical significance was determined by one-way ANOVA with Tukey's post hoc test; ****$P < 0.0001$.



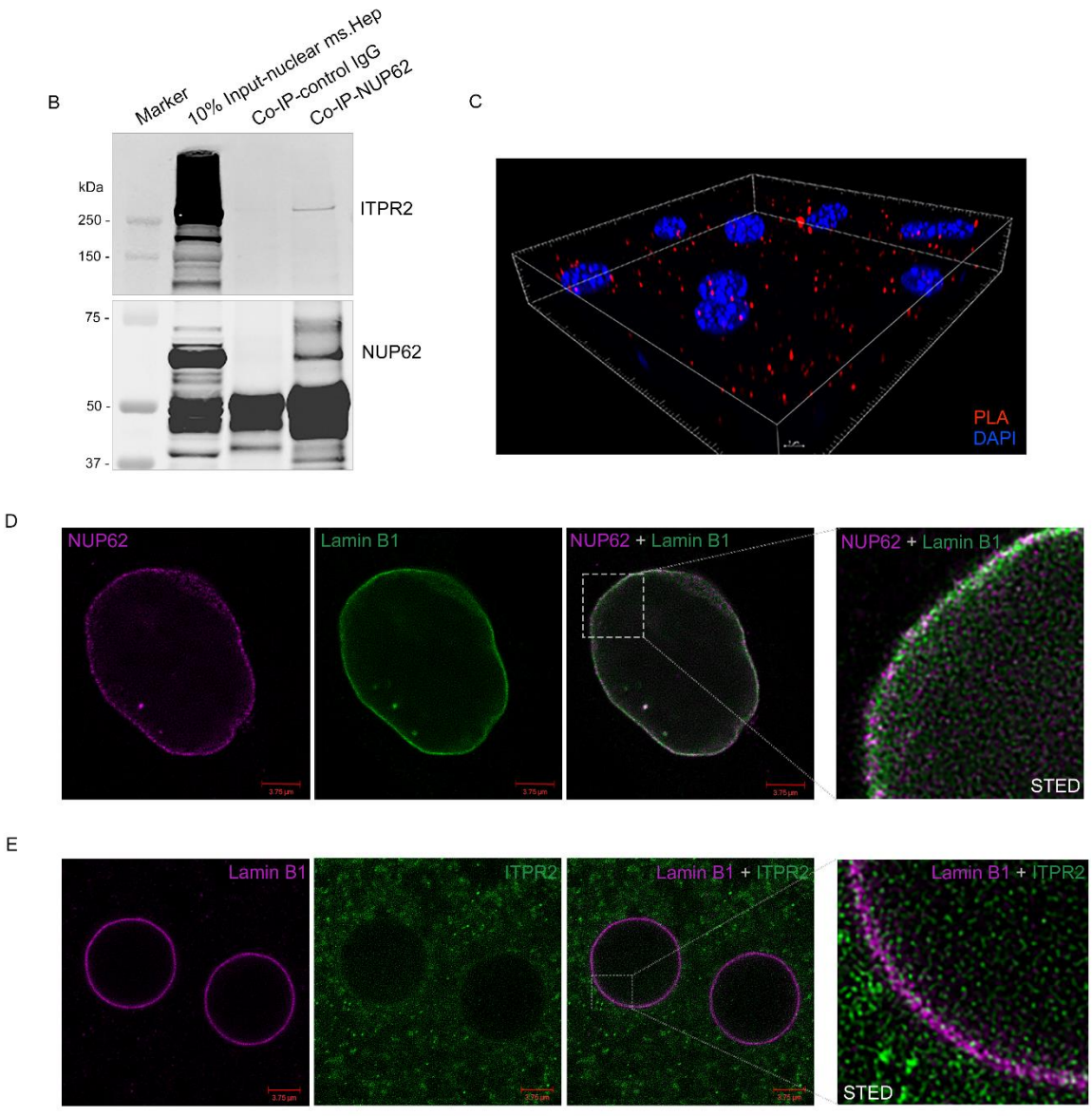
Supplemental Figure 3. Validation of the specificity of ITPR2 antibody in mouse liver sections. (**A**) Representative immunofluorescence staining of liver sections from wild-type and *Itpr2*$^{-/-}$ mice stained with an antibody against ITPR2. Specific ITPR2 immunostaining (*red*) is detected in wild-type but is completely absent in *Itpr2*$^{-/-}$ liver tissues, demonstrating the specificity of the ITPR2 antibody. Nuclei were counterstained with Hoechst 33342 (*blue*). Scale bar: 10 μm. (**B**) Immunoblot analysis of total protein lysate from livers of wild-type and *Itpr2*$^{-/-}$ mice. ITPR2 is detected in wild-type lysates but is absent in *Itpr2*$^{-/-}$ lysates, confirming the specificity of the ITPR2 antibody. GADPH served as the loading control.



Supplemental Figure 4. Validation of ITPR2 antibody specificity in a wild-type and ITPR2-KO liver cell line. (**A**) Representative immunofluorescence images of wild-type (WT) and ITPR2-KO HepG2 cells stained with an antibody against ITPR2. Specific ITPR2 immunoreactivity (*green*) is detected in WT-HepG2 cells but is completely absent in ITPR2-KO HepG2 cells, confirming the specificity of the ITPR2 antibody. Nuclei were counterstained with Hoechst 33342 (*blue*). Scale bar: 10 μm. (**B**) Western blot analysis of total protein lysate from WT and ITPR2-KO HepG2 cells. ITPR2 is detected in WT lysates but is absent in ITPR2-KO HepG2 lysates, further confirming the specificity of the ITPR2 antibody. GADPH served as the loading control.

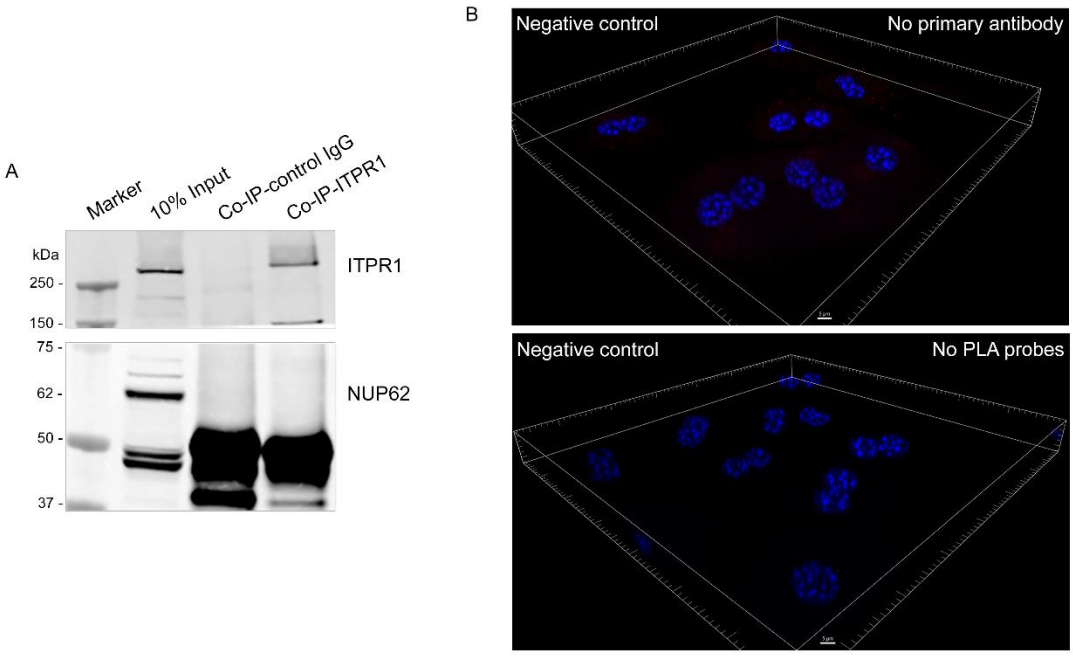
A Nuclear Co-IP-MS analysis of ITPR2-associated proteins in mouse hepatocytes

Accession Number	Protein Name	Alternate ID
Q63850	Nuclear pore glycoprotein p62	NUP62
Q8BTS4	Nuclear pore complex protein Nup54	NUP54
Q8R332	Nucleoporin p58/p45	NUP58

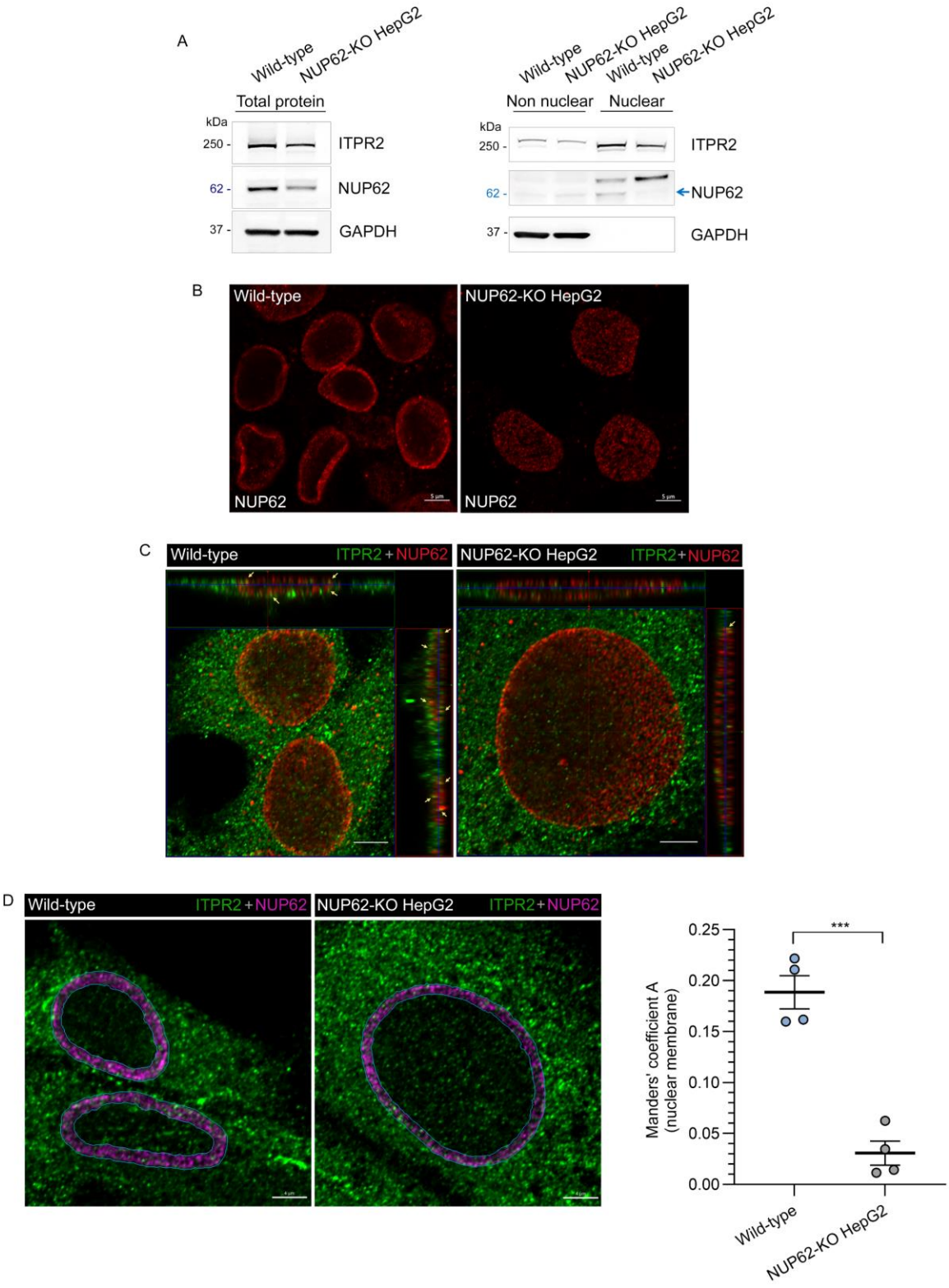


Supplemental Figure 5. Identification of NUP62 as an ITPR2-interacting nuclear protein in primary mouse hepatocytes. (**A**) Summary of results from co-immunoprecipitation (co-IP/mass spectrometry (MS) analyses indicates 3 nuclear pore protein candidates among the top 15 potential nuclear ITPR2-interacting proteins. The nuclear fraction of primary mouse hepatocytes was immunoprecipitated with ITPR2 antibody or control IgG isotope. The resulting MS dataset

was processed and analyzed using Scaffold Proteomics software. (**B**) ITPR2 and NUP62 interact as shown by co-immunoprecipitation (co-IP). Lysates from the nuclear fraction of mouse hepatocytes were immunoprecipitated with NUP62 or isotope control (IgG), followed by immunoblotting with anti-ITPR2 antibody. Input (10%) represents total lysate. Data are representative of 3 independent experiments. (**C**) Detection of ITPR2-NUP62 interaction in mouse hepatocytes by *in situ* proximity ligation assay (PLA) and 3D reconstruction. Representative 3D reconstruction of the z-stack of confocal images of PLA in mouse hepatocytes reveals the spatial distribution of the PLA signal in hepatocytes. PLA puncta signals (*red*) indicating close proximity of ITPR2 and NUP62 were localized in the nucleus and nuclear membrane regions. Nuclei are stained with DAPI (*blue*). Images are representative of 11 observations. Scale bar: 5 μm. (**D**) Co-localization of NUP62 and Lamin B1 revealed by gSTED super-resolution microscopy**.** The gSTED images demonstrate the subcellular localization and spatial overlap of NUP62 (*magenta*) and Lamin B1 (*green*) in isolated mouse hepatocytes. (**E**) Co-localization of Lamin B1 and ITPR2 demonstrated by gSTED microscopy**.** The gSTED images illustrate the subcellular localization and spatial overlap of Lamin B1 (*magenta*) and ITPR2 (*green*) in isolated mouse hepatocytes. Merged images show spatial co-localization (*white*) at nuclear membrane region. Scale bar: 3.75 μm. Due to the lack of suitable immunofluorescence compatible antibodies for ITPR2 and NUP62 in mouse hepatocytes, direct co-immunostaining of these two proteins could not be performed. Instead, co-staining of NUP62 with Lamin B1, as well as Lamin B1 with ITPR2, was conducted.

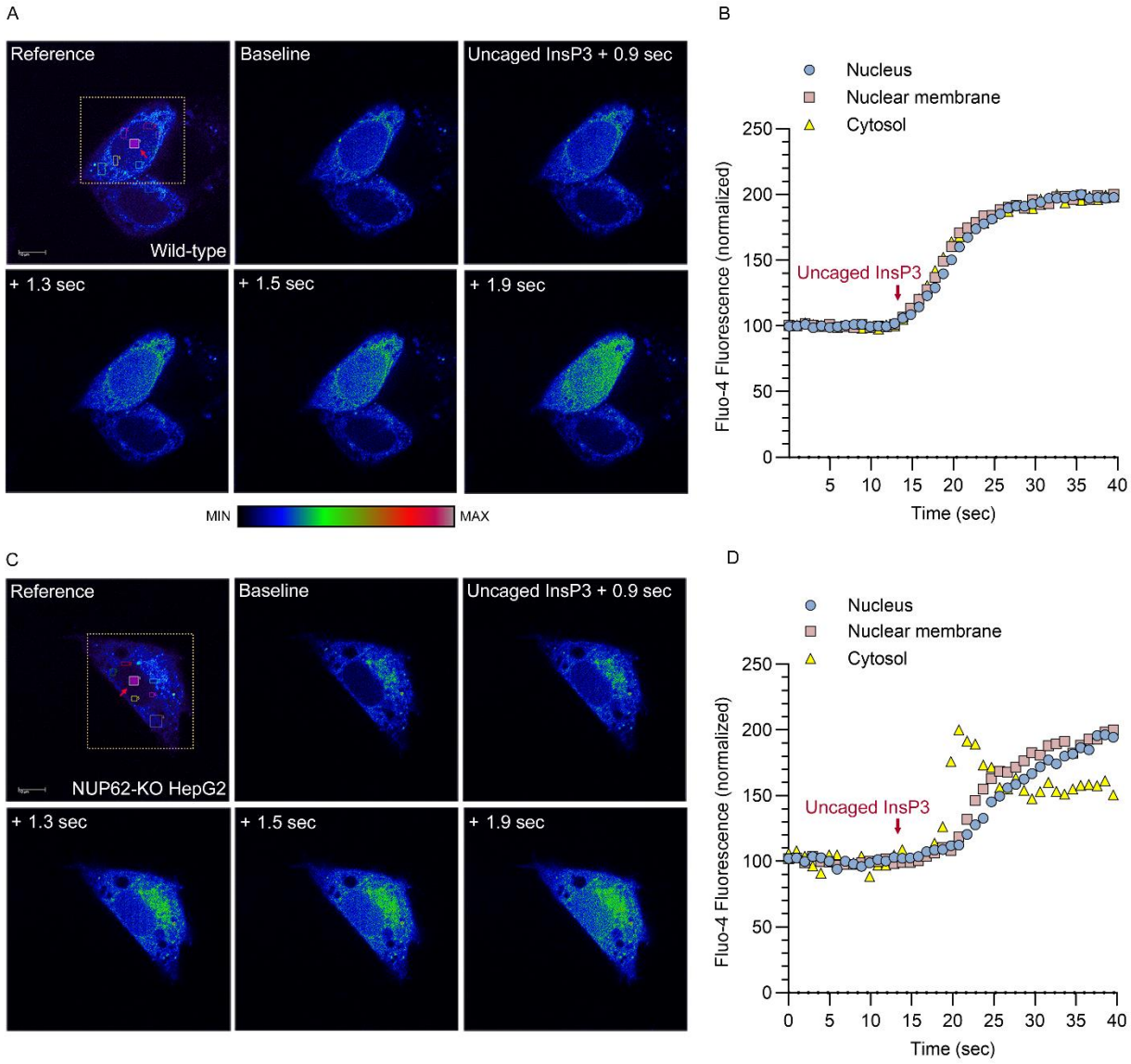


Supplemental Figure 6. Isoform-specific interaction of ITPR2 with NUP62. (**A**) Representative co-immunoprecipitation (co-IP) analysis demonstrating that ITPR1 does not associate with NUP62 under the same experimental conditions used for ITPR2. Lysates from nuclear fraction of mouse hepatocytes were immunoprecipitated with ITPR1 or antibody control (IgG), followed by immunoblotting with anti-NUP62 antibody. Input (10%) represents total lysate. (**B**) Representative 3D reconstruction of the z-stack of confocal images of negative controls for the proximity ligation assay (PLA) in mouse hepatocytes. Nuclei are stained with DAPI (*blue*). Scale bar: 5 μm. Omission of either the primary antibody (*top panel*) or the PLA probes (*bottom panel*) abolished the PLA signal, with only minimal background fluorescence observed, confirming the specificity of the PLA detection.

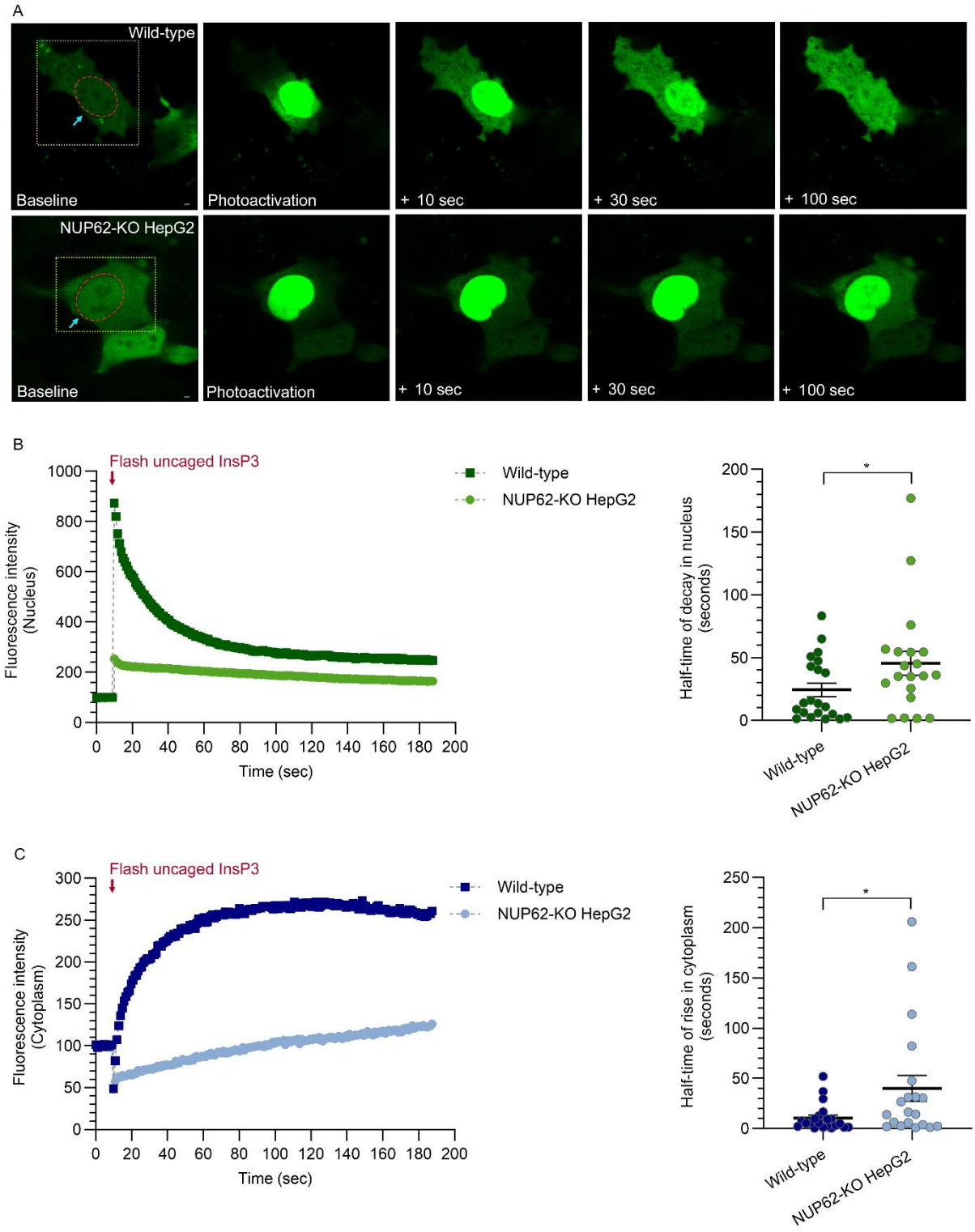


Supplemental Figure 7. Validation of CRISPR/Cas9-mediated knockout of NUP62 in HepG2 cells. (**A**) Representative immunoblot of total whole cell, non-nuclear, and nuclear fractions for NUP62 expression. Western blots show the near absence of NUP62 in NUP62-KO HepG2 cells

compared to wild-type cells. GAPDH served as a loading control and a marker for non-nuclear purity. The arrow denotes the expected molecular weight of NUP62, demonstrating the absence of the NUP62 band in NUP62-KO cells. (**B**) Immunofluorescence staining of NUP62 in wild-type and NUP62-KO HepG2 cells confirms loss of NUP62 at the nuclear membrane/nuclear pore region in NUP62-KO HepG2 cells. Scale bar: 5 μm. (**C**) Airyscan confocal microscopy reveals differential co-localization of ITPR2 (*green*) and NUP62 (*red*) at the nuclear membrane in wild-type and NUP62-KO HepG2 cells. Z-stack images of wild-type and NUP62-KO HepG2 cells were acquired using Airyscan high-resolution confocal microscopy and displayed as orthogonal (XZ and YZ) views. Merged images illustrate spatial co-localization (*yellow*) within the nuclear membrane. Yellow arrows indicate representative localized puncta. Scale bar: 5 μm. (**D**) Representative confocal microscopy of co-localization of ITPR2 and NUP62 at the nuclear membrane in wild-type and NUP62-KO HepG2 cells (*left panel*). Z-stack images were acquired using Airyscan high-resolution confocal microscopy. Co-localization analysis was performed using Imaris software, focusing specifically on the nuclear membrane region, which was segmented and masked by a line (*cyan*) to delineate the region of interest (ROI). Scale bar: 4 μm. *Right panel*: Quantitative co-localization parameter (Manders' coefficient) shows a significant decrease in co-localization of ITPR2 and NUP62 in the ROI of NUP62-KO cells. Manders' coefficient was calculated within the nuclear membrane ROI (*cyan*) and used to compare wild-type and NUP62-KO HepG2 cells. Values reflect individual data points ± SEM from four z-stack confocal images. Statistical significance was determined by a two-tailed unpaired t-test; ****P* = 0.0002.

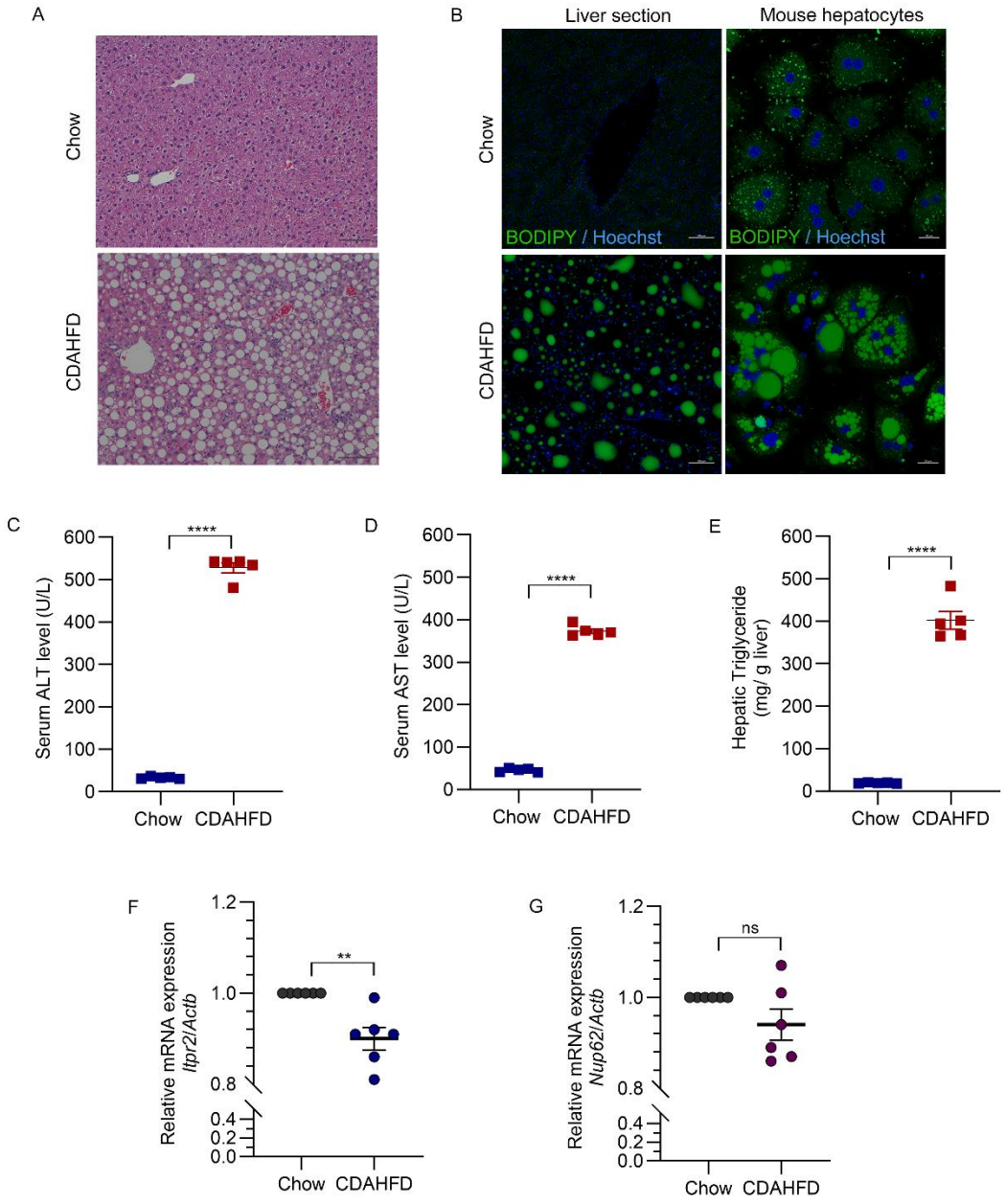


Supplemental Figure 8. The origin of InsP3-induced nuclear Ca^{2+} signals changes in NUP62-KO HepG2 cells. Serial confocal images and corresponding tracings of InsP3-induced Ca^{2+} transients in the nucleus of (**A-B**) wild-type HepG2 and (**C-D**) NUP62-KO HepG2 cells. Cells were loaded with caged InsP3 (ci-InsP3) and Fluo-4/AM. ci-InsP3 was photo-released within the designated region (small white square with an arrow) in the middle of the nucleus as shown in a reference image of the selected cell (dotted large square) by a controlled near-UV (405 nm) flash as the induced nuclear Ca^{2+} signal was monitored by time-lapse swept-field confocal microscopy. A pseudo-colored Ca^{2+} scale is shown. Scale bar: 10 μm. Ca^{2+} signal analysis across the intra-nuclear, nuclear membrane, and cytoplasmic regions in (B) and (D) are normalized to the same baseline and peak values to facilitate comparison of the two curves. Ca^{2+} transients originated nearly simultaneously at and near the nuclear membrane in wild-type HepG2 cells, while Ca^{2+} signals begin in the cytosol before spreading into the nucleus in NUP62-KO HepG2 cells. Images are representative of what was observed in 8 cells in each group.



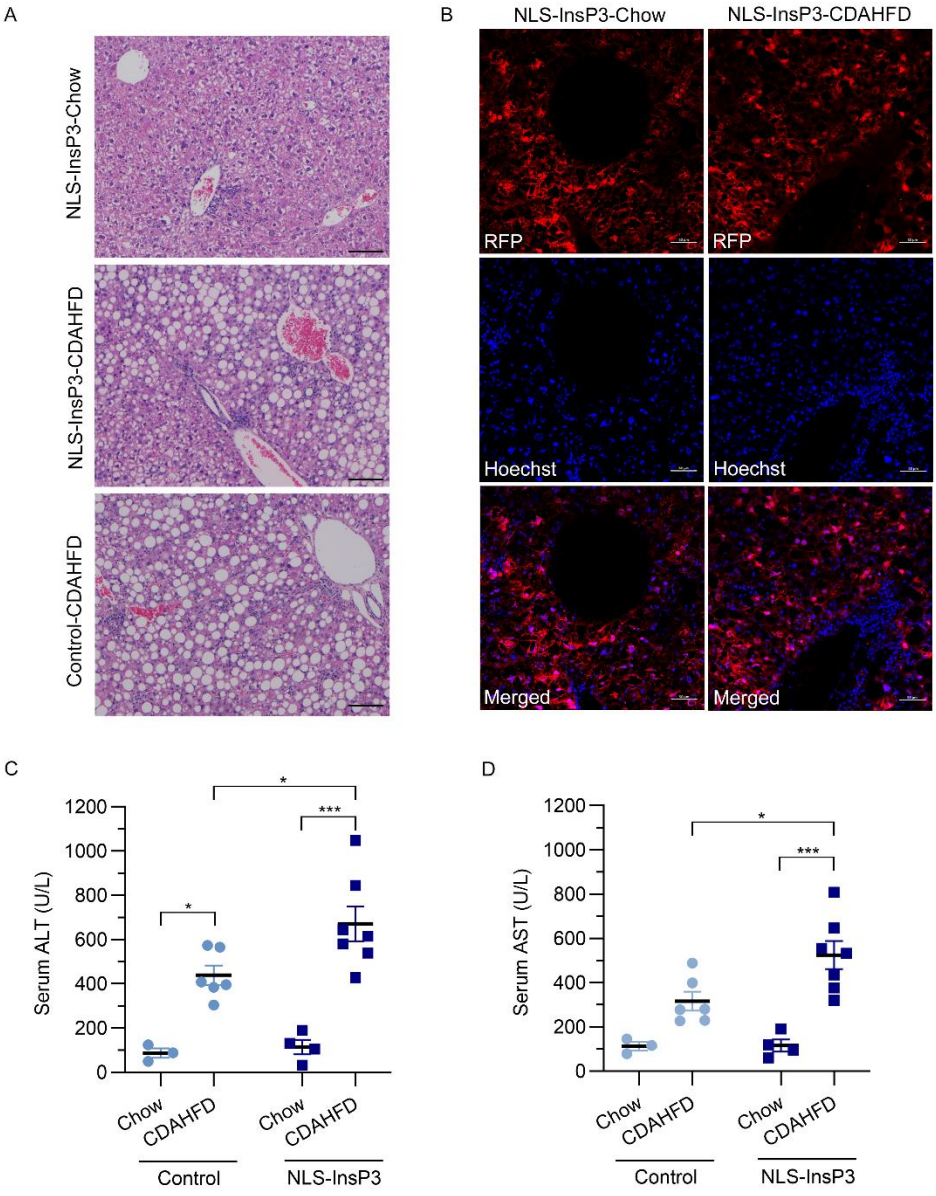
Supplemental Figure 9. Loss of NUP62 is associated with decreased nuclear pore permeability. (**A**) Time-lapse images of photoactivatable GFP (PA-GFP) released in the nucleus of a representative wild-type (*top panel*) and NUP62-KO (*bottom panel*) HepG2 cell. GFP can be detected sooner in the cytoplasm of the wild-type cell. Cells were co-transfected with PA-GFP

and a red fluorescent protein (mRFP) for identification, and the GFP was photoactivated in the center region of the nucleus (dotted ellipse and indicated with arrows) by a controlled near-UV (405 nm) flash. Fluorescence intensity was monitored across the cell over a period of 180 seconds. Scale bar: 10 μm. (**B**) GFP is lost from the nucleus more rapidly in wild-type cells. *Left panel*: fluorescence intensity tracing from representative wild-type and NUP62-KO cells showing the decrease in GFP fluorescence in the nucleus over time. *Right panel*: Quantification of the half-time of fluorescence decay in the nucleus. (**C**) GFP moves to the cytoplasm more quickly in wild-type cells. *Left panel*: fluorescence intensity tracing from representative wild-type and NUP62-KO cells showing the increase in GFP fluorescence in the cytoplasm over time. *Right panel*: Quantification of the half-time of fluorescence rise in the cytoplasm, indicating redistribution of GFP. Data represents 3 independent experiment with 20-21 cells. Values reflect individual data points and mean ± SEM. Statistical significance was determined by a one-tailed unpaired t-test; $*P < 0.05$ for comparisons between groups.



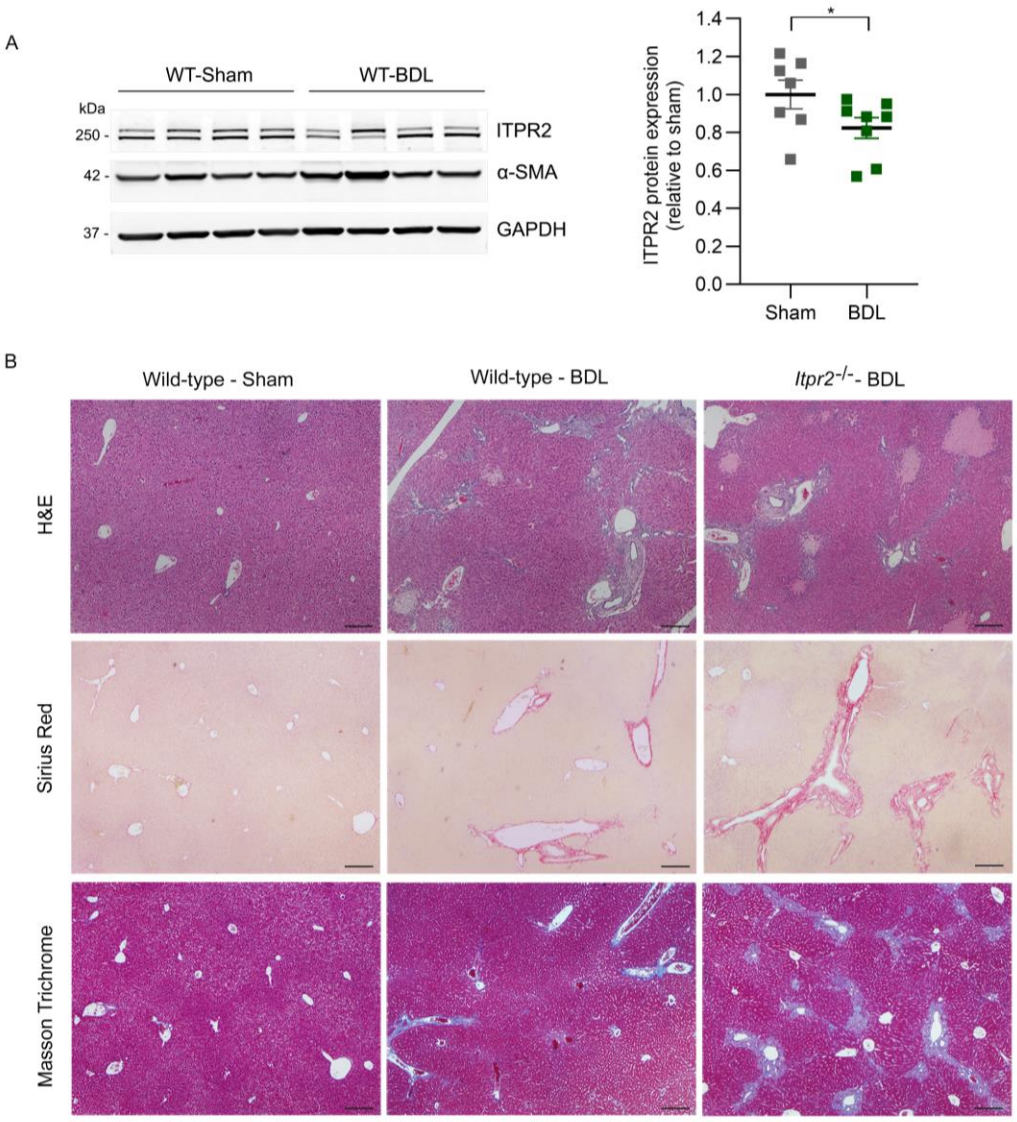
Supplemental Figure 10. CDAHFD feeding induces steatohepatitis and liver injury and impairs nuclear Ca^{2+} signaling in hepatocytes. (**A**) Representative hematoxylin and eosin staining of liver sections from chow diet (*top*) and CDAHFD mice (*bottom*) for 4 weeks reveals steatosis and inflammation in the latter. Scale bar: 100 μm. (**B**) Immunofluorescence staining of liver sections using BODIPY 493/503 (*green*) shows marked lipid droplet accumulation in liver sections (*left panel*) and hepatocytes (*right panel*) of CDAHFD-fed mice compared to control chow diet. Hoechst (*blue*) was used for nuclear staining. Scale bar: 100 μm (liver sections), Scale bar:

20 μm (mouse hepatocytes). (**C**) Serum levels of alanine aminotransferase (ALT), (**D**) Serum levels of aspartate aminotransferase (AST), and (**E**) hepatic triglyceride levels were measured after 4 weeks of CDAHFD feeding. CDAHFD-fed mice showed significant elevations of ALT, AST levels along with increased triglyceride levels. Data represent mean ± SEM, n=5 per group. Statistical significance was determined by a two-tailed unpaired t-test; ****$P < 0.0001$. Relative mRNA expression of (**F**) *Itpr2* and (**G**) *Nup62* in hepatocytes isolated from chow- or CDAHFD-fed mice. CDAHFD significantly reduced *Itpr2* mRNA expression, whereas *Nup62* expression was unchanged. Data represent mean ± SEM, n=6 per group. Statistical significance was determined by a two-tailed unpaired t-test; **$P < 0.01$; ns, not significant.

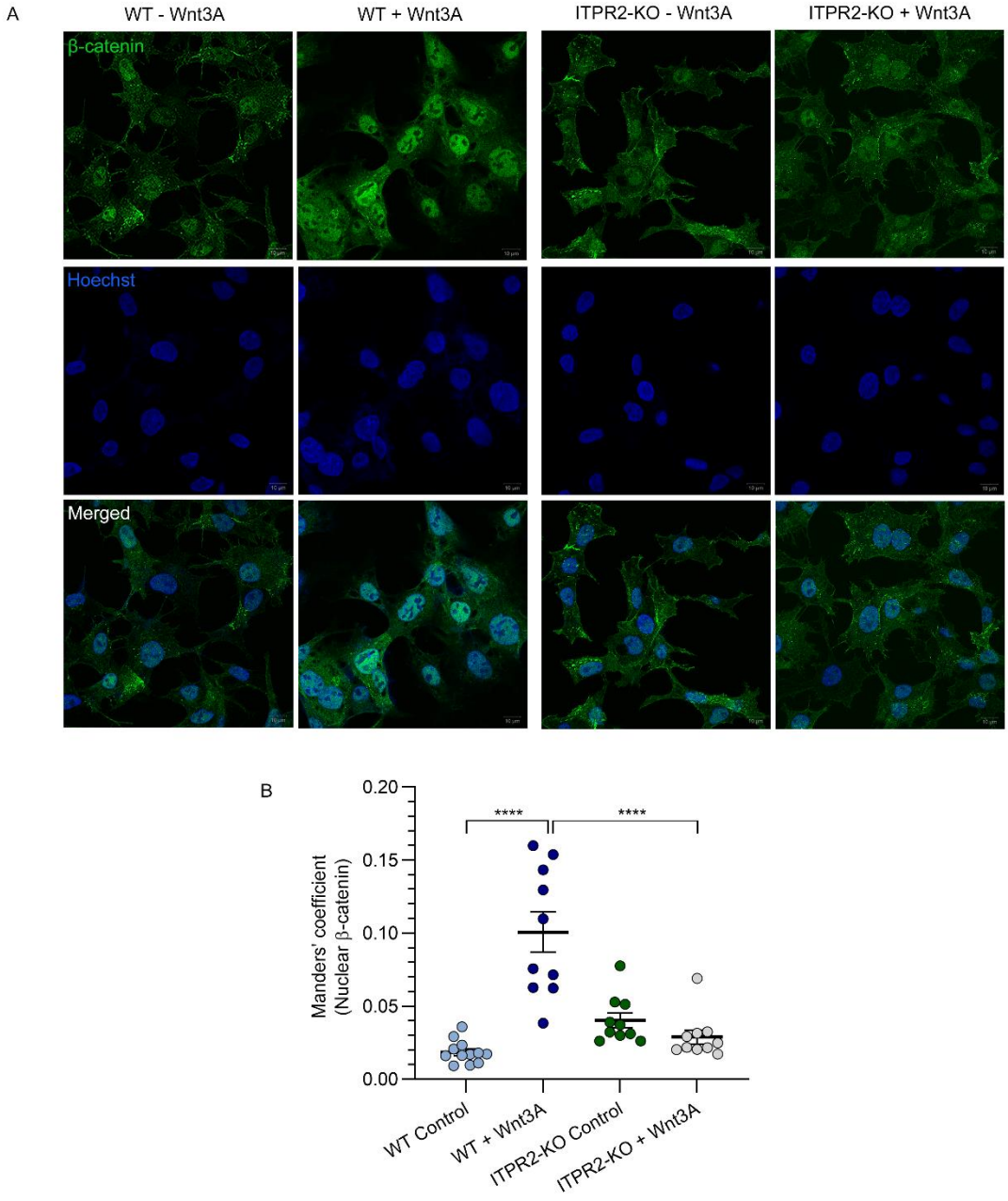


Supplemental Figure 11. Hepatocellular damage in CDAHFD mice is increased by expression of a nuclear InsP3 buffer. (**A**) Representative hematoxylin and eosin of liver sections from mice expressing the nuclear InsP3 buffer construct fed a chow diet (NLS-InsP3-chow) (*top panel*) or CDAHFD (NLS-InsP3-CDAHFD) (*middle panel*) and mice (control) fed a CDAHFD (*bottom panel*) for 2 weeks. Scale bar: 100 μm. (**B**) Confirmation of adenovirus construct encoding InsP3 fused to a nuclear localization signal (NLS) delivery to the liver following tail vein injection. Representative fluorescence images of liver sections from mice injected with adenovirus expressing nuclear InsP3 buffer construct (NLS-InsP3) subjected to chow diet or CDAHFD feeding. Red fluorescent protein (RFP) intensity indicates successful transduction of hepatocytes,

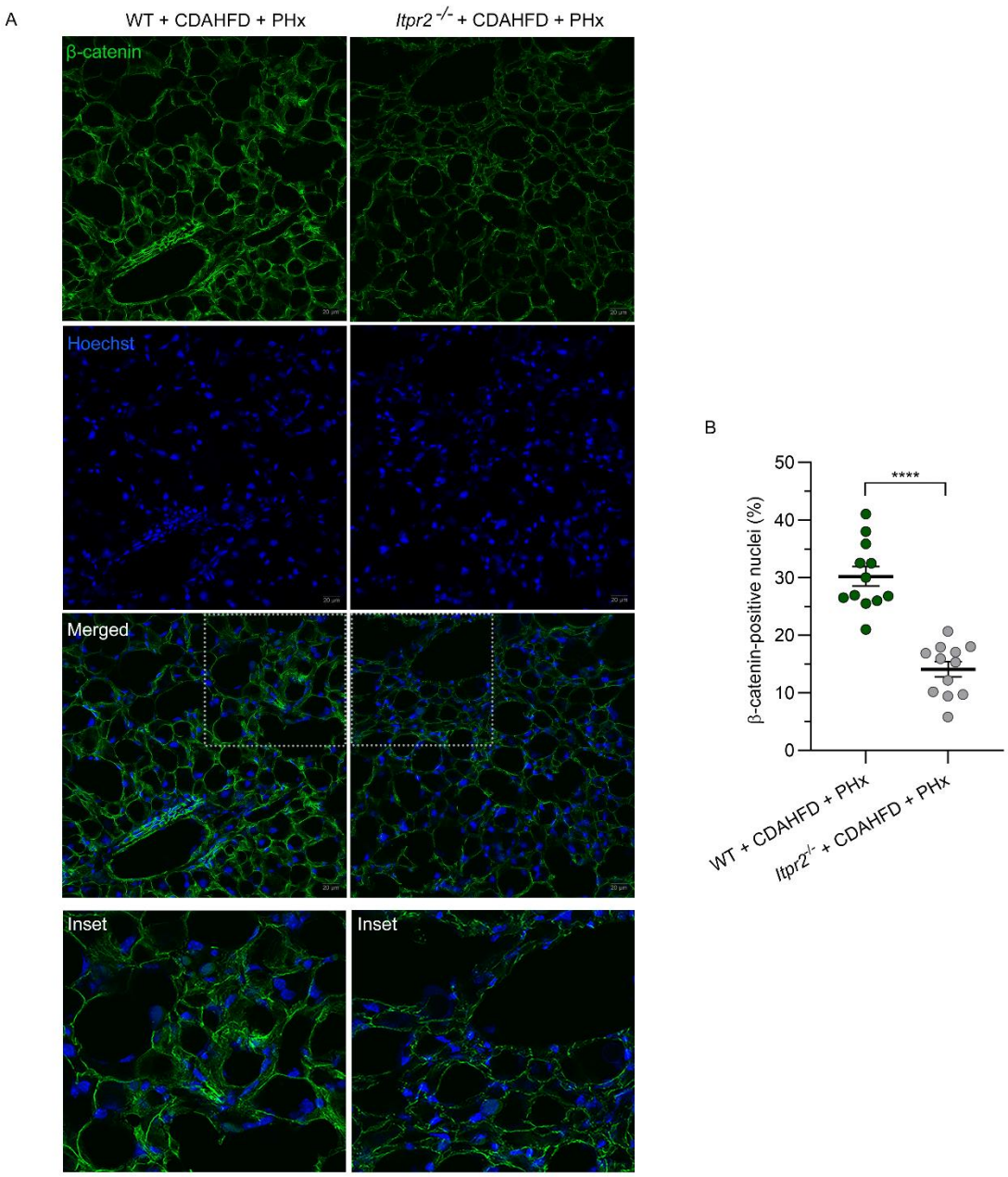
confirming the liver-specific delivery of the adenovirus expressing nuclear InsP3 buffer construct. Images were taken 2 weeks after chow or CDAHFD feeding. Scale bar: 50 μm. (**C**) Serum ALT and (**D**) serum AST levels are significantly higher in mice expressing nuclear InsP3 buffer (NLS-InsP3) and fed with a CDAHFD for 2 weeks than CDAHFD-fed control mice. Data represent mean ± SEM from chow control diet (n=3), chow control diet with NLS-InsP3 (n=4 mice) and CDAHFD group (n=6), CDAHFD with NLS-InsP3 (n=7). Statistical significance was determined by one-way ANOVA with Tukey's post hoc test; *$P < 0.05$, ***$P < 0.001$ as indicated for the compared groups.



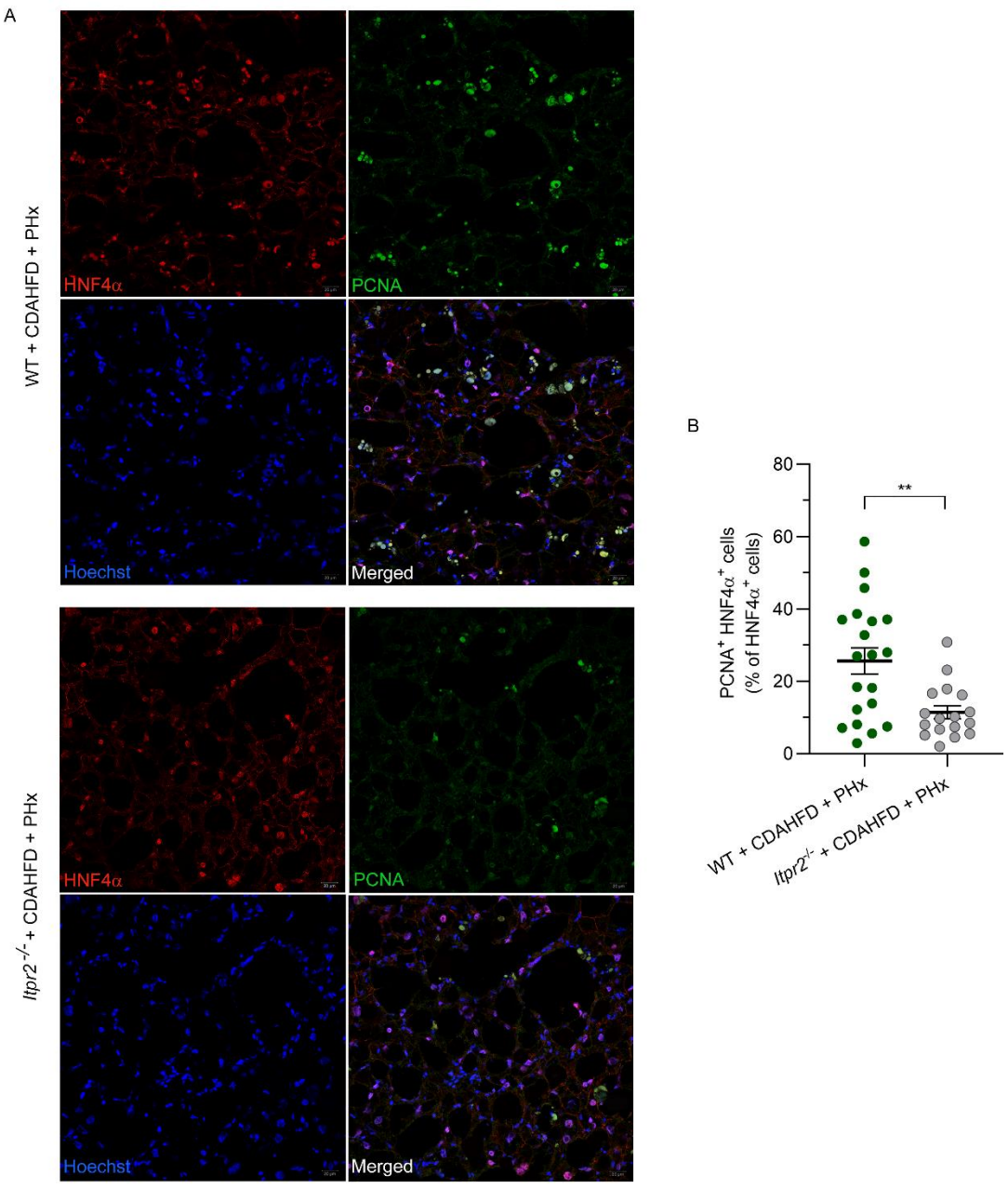
Supplemental Figure 12. Bile duct ligation induces liver fibrosis and reduces ITPR2 protein expression. (**A**) Immunoblot analysis of liver lysates from sham-operated control mice and wild-type (WT) mice subjected to bile duct ligation (BDL) for 2 weeks (*left panel*). BDL mice show a reduction in ITPR2 levels along with increased expression of α-smooth muscle actin (α-SMA), a marker of fibrosis, compared to sham controls. GAPDH was used as a loading control. Densitometric quantification of ITPR2 expression (*right panel*) is shown relative to sham mice. Protein levels of ITPR2 are significantly diminished in BDL mice compared to sham controls. Data represent mean ± SEM, sham (n=7) and BDL (n=8). Statistical significance was determined by a one-tailed unpaired t-test; $*P < 0.05$ for comparisons between groups. (**B**) Representative hematoxylin and eosin (H&E), Sirius Red, and Masson Trichrome staining of liver sections from sham-operated control, wild-type mice following BDL, and *Itpr2*$^{-/-}$ mice following BDL for 2 weeks. Livers from BDL mice show characteristic features of fibrosis, including hepatocellular damage, inflammatory cell infiltration, and bile duct proliferation. Scale bar: 200 μm.



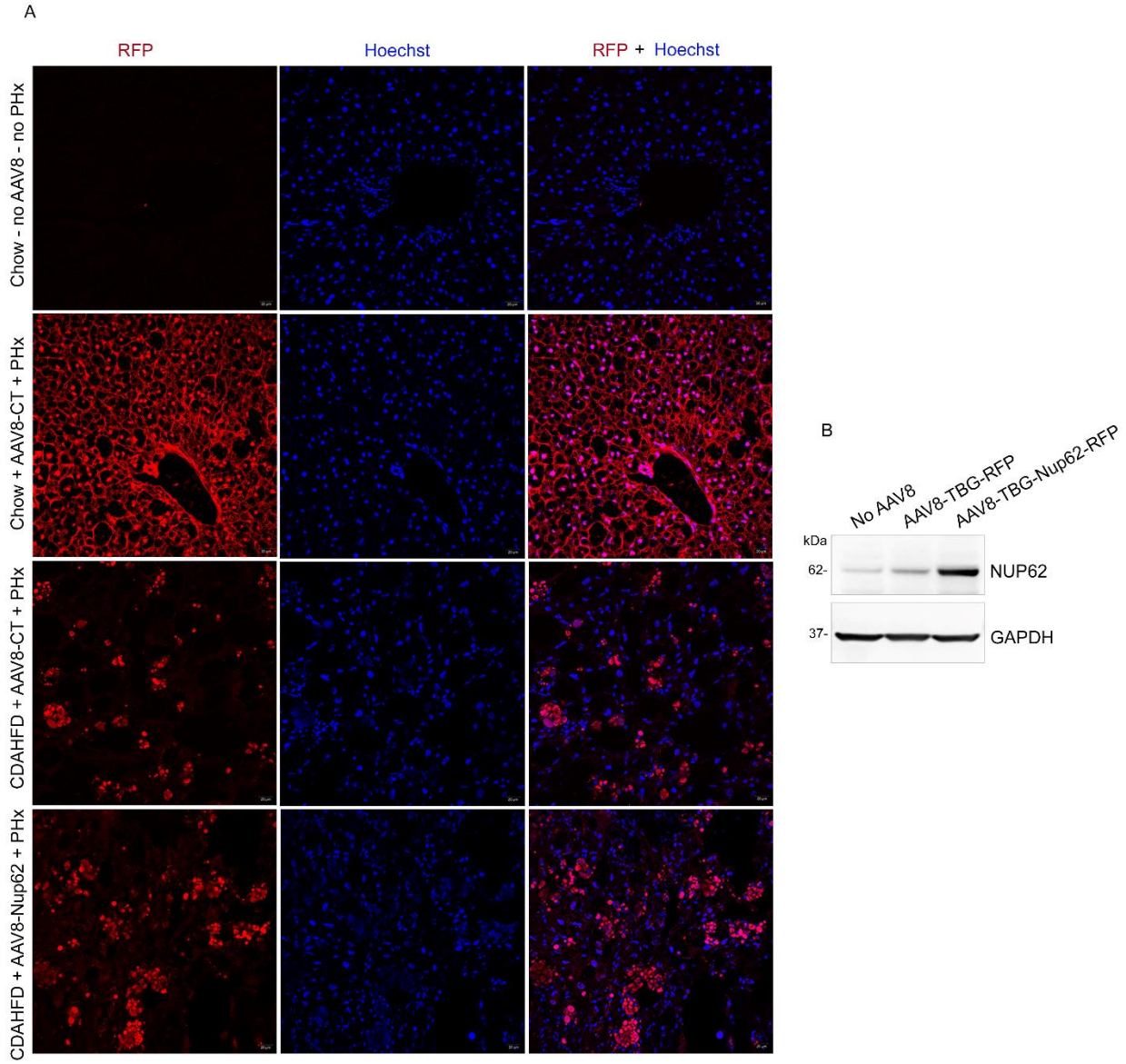
Supplemental Figure 13. Loss of ITPR2 diminishes Wnt3A-induced nuclear β-catenin accumulation. (**A**) Representative immunofluorescence images of wild-type (WT) and ITPR2-KO HepG2 cells under basal conditions or following Wnt3A stimulation. β-catenin is shown in *green* and nuclei are stained with Hoechst (*blue*). Wnt3A stimulation promoted nuclear accumulation of β-catenin in WT cells, whereas this response was markedly reduced in ITPR2-KO cells. (**B**) Quantitation of β-catenin nuclear localization using Manders' colocalization coefficient confirms that Wnt3A-induced translocation of β-catenin is reduced in the absence of ITPR2. Values represent individual data points ± SEM from 10 confocal images. Statistical significance was determined by one-way ANOVA with Tukey's post hoc test; ****$P < 0.0001$. Scale bar: 10 μm.



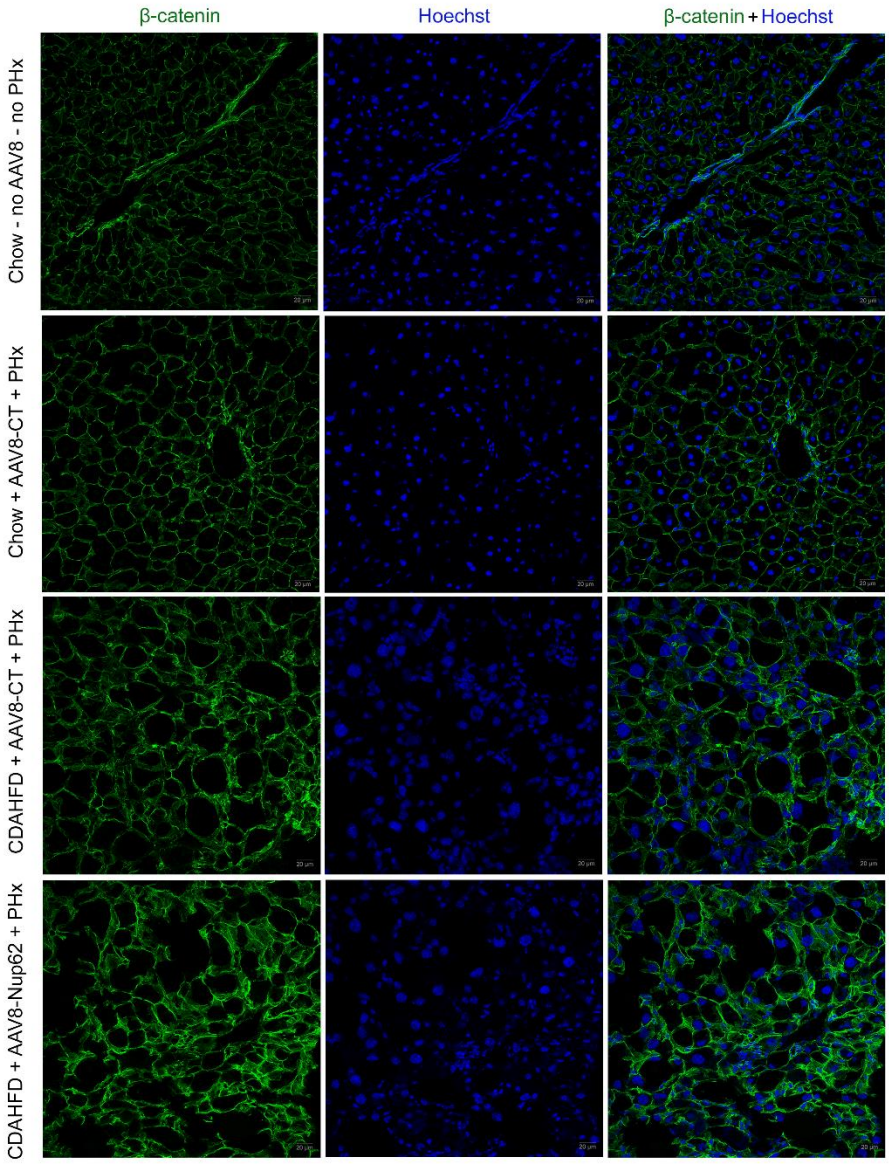
Supplemental Figure 14. Loss of ITPR2 impairs nuclear β-catenin localization after CDAHFD and partial hepatectomy. (**A**) Representative immunofluorescence images of liver sections from wild-type (WT) and *Itpr2*$^{-/-}$ mice fed a CDAHFD followed by 70% partial hepatectomy (PHx) stained for β-catenin (*green*) and nuclei (Hoechst, *blue*). Scale bar: 20 μm. Liver sections from WT mice subjected to a CDAHFD and PHx exhibited more nuclear accumulation of β-catenin compared with *Itpr2*$^{-/-}$ mice subjected to the same treatment. (**B**) Quantification of the percentage of β-catenin-positive nuclei confirms this difference. Data are presented as mean ± SEM, n=4 mice per group. Three randomly selected fields were analyzed per mouse. The inset shows a magnified view of the highlighted region (gray box) with merged β-catenin and Hoechst (nuclei) fluorescence. Statistical significance was determined by a two-tailed unpaired t-test; ****P < 0.0001.



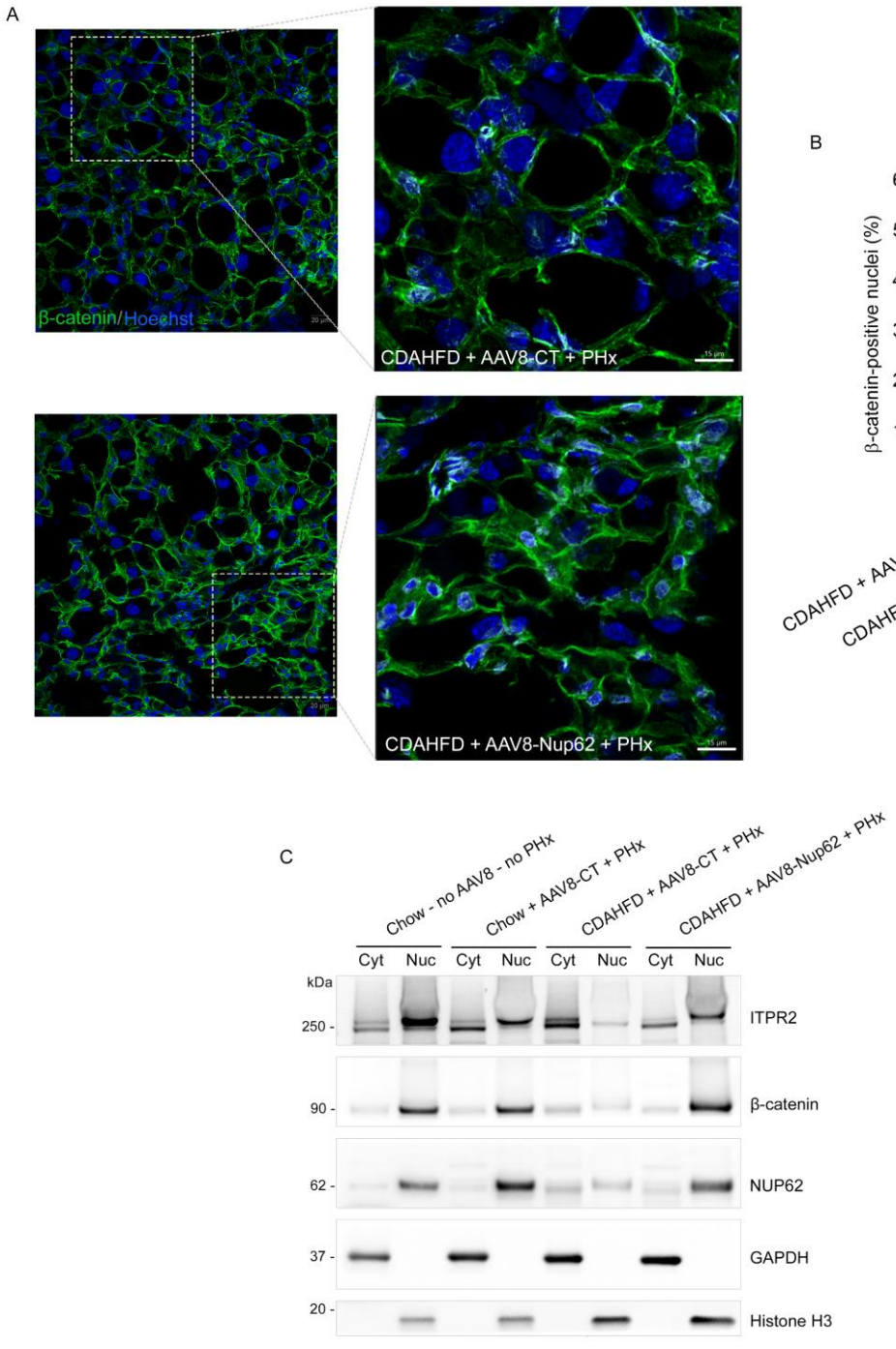
Supplemental Figure 15. Loss of ITPR2 reduces hepatocytes proliferation after CDAHFD and partial hepatectomy. (**A**) Representative immunofluorescence images of liver sections stained for PCNA (*green*), HNF4α (*red*), and Hoechst (*blue*) from wild-type (WT) and *Itpr2*$^{-/-}$ mice fed a CDAHFD and subjected to 70% partial hepatectomy (PHx). PCNA-positive hepatocytes were identified as PCNA^{+} HNF4α^{+} double positive cells. Scale bar: 20 μm. WT mice subjected to a CDAHFD and PHx exhibited a higher number of PCNA^{+} HNF4α^{+} cells than *Itpr2*$^{-/-}$ mice. (**B**) Quantification of PCNA^{+} HNF4α^{+} hepatocytes expressed as a percentage of total HNF4α^{+} hepatocytes confirm this difference. Data represent mean ± SEM, n=4 per group, five randomly selected fields were analyzed per mouse. Statistical significance was determined by a two-tailed unpaired t-test; ***P* = 0.0016.



Supplemental Figure 16. Hepatocyte-specific AAV8-mediated Nup62 expression in mice. (**A**) Representative immunofluorescence images of liver sections from mice intravenously injected with AAV8-TBG-Nup62-RFP or AAV8-TBG-RFP (control; AAV8-CT) via the tail vein. Red fluorescent protein (RFP) fluorescence was detected in hepatocytes, confirming efficient hepatocyte transduction. Nuclei were counterstained with Hoechst (*blue*). Scale bar: 20 μm. (**B**) Representative Western blot analysis of liver lysates demonstrated increased NUP62 expression in AAV8-Nup62-treated mice 1-week after AAV8 delivery. GAPDH was used as a loading control.

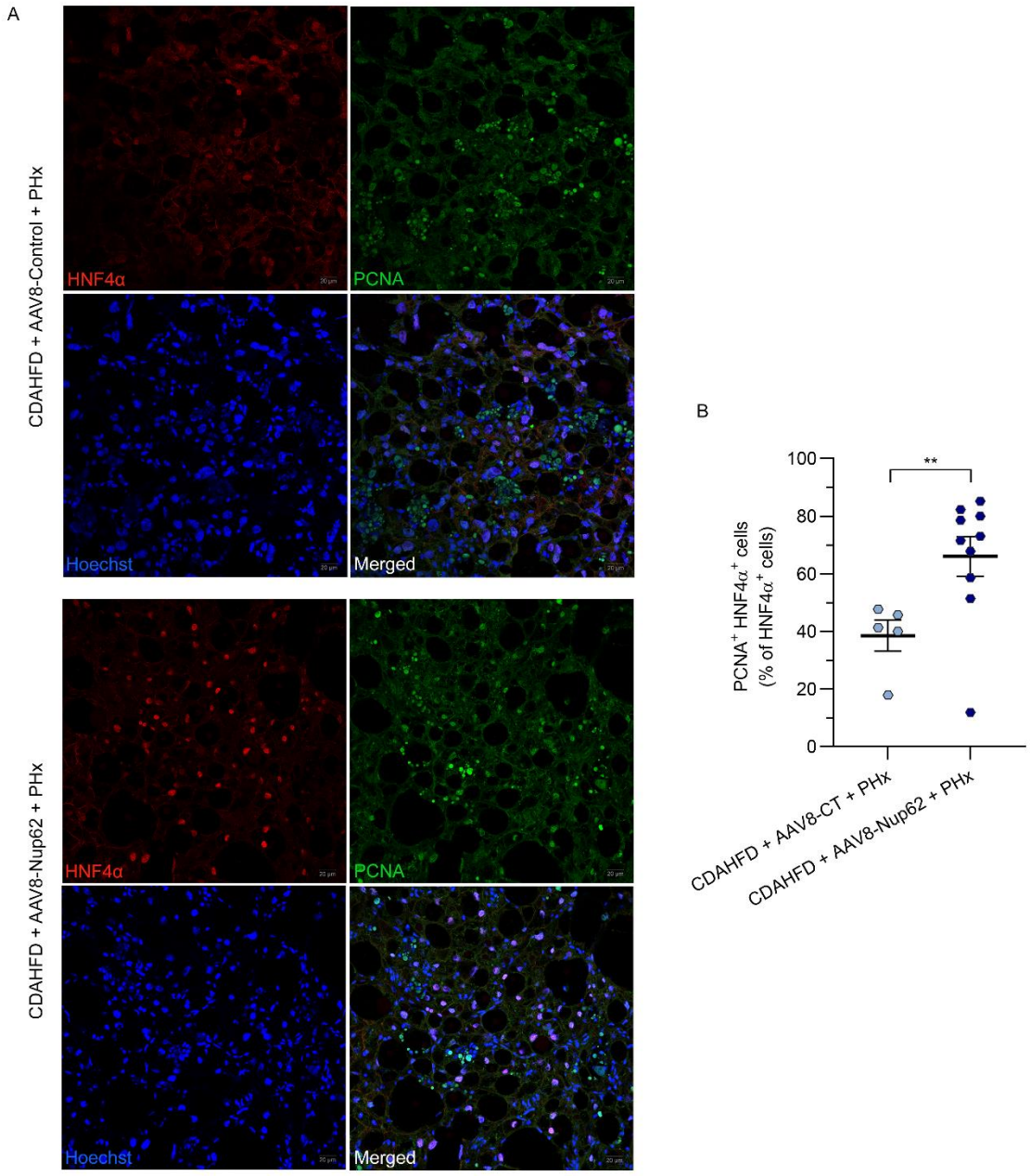


Supplemental Figure 17. Restoration of NUP62 promotes nuclear β-catenin localization following CDAHFD and partial hepatectomy. Representative immunofluorescence images of liver section stained for β-catenin (*green*) and nuclei (Hoechst, *blue*) from mice in the following experimental groups: (*top row*) Chow diet, no AAV8, no partial hepatectomy (PHx); (*second row*) Chow diet + AAV8-TBG-RFP + PHx; (*third row*) CDAHFD + AAV8-TBG-RFP + PHx; and (*bottom row*) CDAHFD + AAV8-TBG-Nup62-RFP + PHx. CDAHFD-fed mice receiving AAV8-control exhibited a much smaller increase in nuclear accumulation of β-catenin compared to AAV8-Nup62 groups. Scale bar: 20 μm. AAV8-CT denotes AAV8-TBG-RFP (control).



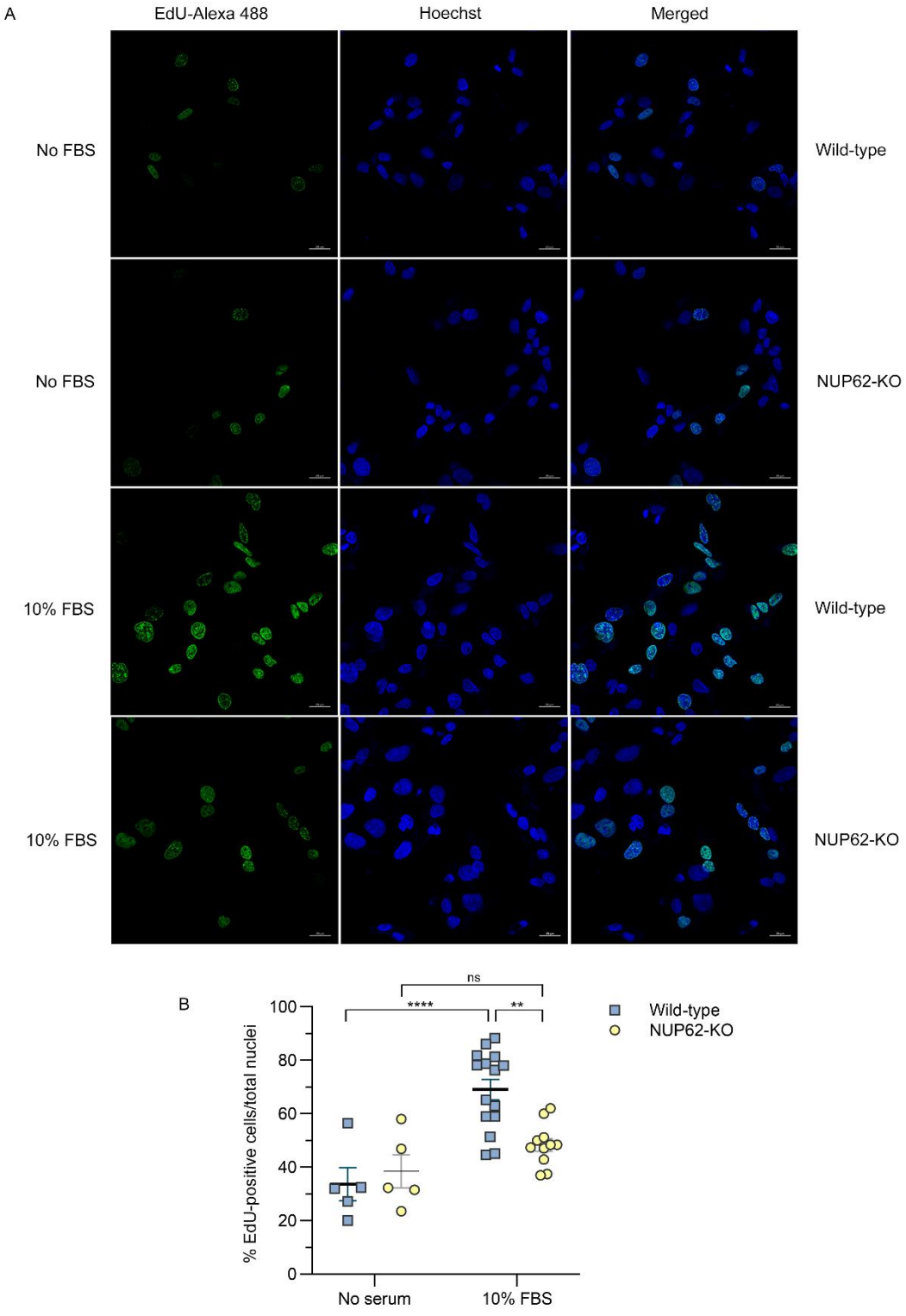
Supplemental Figure 18. NUP62 restoration enhances nuclear β-catenin accumulation in hepatocytes following CDAHFD and partial hepatectomy. (**A**) Magnified representative immunofluorescence images of liver sections from CDAHFD + AAV8-TBG-RFP (control; AAV8-CT) + PHx and CDAHFD + AAV8-TBG-Nup62-RFP + PHx, stained for β-catenin (*green*) and nuclei (Hoechst, *blue*) as shown in the Supplemental Figure 17. Representative pseudo-color

image generated by Imaris colocalization analysis illustrating the spatial overlap β-catenin (*green*) and nuclei (*blue*) is shown. Colocalized signal are shown in *white*. Scale bar: 15 μm. (**B**) Quantification of the percentage of β-catenin-positive nuclei in CDAHFD-fed mice receiving AAV8-control or AAV8-Nup62 following partial hepatectomy. Values reflect individual data points ± SEM from 9 images from the single surviving mouse from the CDAHFD + AAV8-control + PHx group and 15 images from the 3 surviving mice of the CDAHFD + AAV8-Nup62 + PHx group. Statistical significance was determined by a two-tailed unpaired t-test; $^{**}P < 0.01$. (**C**) Representative Western blot analysis of cytosolic and nuclear fractions isolated from liver tissue. The expression of β-catenin in the nucleus fraction was reduced in CDAHFD-fed mice receiving AAV8-control, whereas restoration of NUP62 by AAV8 rescued nuclear accumulation of β-catenin following CDAHFD and PHx.



Supplemental Figure 19. Restoration of NUP62 improves hepatocytes proliferation capacity after CDAHFD and partial hepatectomy. (**A**) Representative immunofluorescence images of liver sections stained for PCNA (*green*), HNF4α (*red*), and Hoechst (*blue*) from CDAHFD-fed mice receiving AAV8-TBG-RFP (control; AAV8-CT) or AAV8-TBG-Nup62-RFP following partial hepatectomy. PCNA-positive hepatocytes were identified as PCNA$^+$ HNF4α$^+$ double positive cells. Scale bar: 20 μm. (**B**) Quantification of PCNA$^+$ HNF4α$^+$ hepatocytes expressed as a percentage of total HNF4α$^+$ hepatocytes. The CDAHFD + AAV8-Nup62 + PHx

group showed a significant higher percentage of $PCNA^+$ $HNF4\alpha^+$ cells than the CDAHFD + AAV8-control + PHx group. Data represent mean ± SEM from 5 images collected from the single surviving mouse of the CDAHFD + AAV8-control + PHx group and 10 images collected from the 3 surviving mice of the CDAHFD + AAV8-Nup62 + PHx group. Statistical significance was determined by a two-tailed unpaired t-test; $^{**}P < 0.01$.



Supplemental Figure 20. Loss of NUP62 decreases EdU incorporation in HepG2 cells. (**A**) Representative confocal image showing EdU-positive nuclei (*green*), indicative of cell proliferation, and total nuclei counterstained with Hoechst 33342 (*blue*) in wild-type and NUP62-

KO HepG2 cells cultured without serum and with 10% fetal bovine serum (FBS) for 24 hours. EdU (10 μm) was added to the culture medium for the final 2 hours of incubation and processed using the Click-iT EdU imaging kit. Scale bar: 20 μm. (**B**) Quantitative analysis of EdU-incorporated cells. EdU staining is markedly reduced in NUP62-KO HepG2 cells. Data are mean ± SEM from three independent coverslips (wild-type without serum, n=5; NUP62-KO, n=5; wild-type with 10% serum, n=15; NUP62-KO with 10% serum, n=11). Statistical significance was determined by two-way ANOVA with Tukey's post hoc test; $^{**}P = 0.0014$, $^{****}P < 0.0001$. Abbreviation: ns, not significant; EdU, 5-ethynyl-2′-deoxyuridine